

The limiting behaviour of turbulence near a wall

By DEAN R. CHAPMAN

Department of Aeronautics and Astronautics, Stanford University, Stanford, CA 94305, USA

AND GARY D. KUHN

Nielsen Engineering & Research, Inc., 510 Clyde Avenue, Mountain View, CA 94043, USA

(Received 30 September 1985 and in revised form 7 March 1986)

Three different Navier–Stokes computational models of incompressible viscous-sublayer turbulence have been developed. Comparison of computed turbulence quantities with experiment is made for the mean streamwise velocity, Reynolds stress, correlation coefficient and dissipation; for the r.m.s. fluctuation intensities of streamwise vorticity, Reynolds stress and three velocity components; and for the skewness and flatness of fluctuating streamwise velocity and Reynolds stress. The comparison is good for the first three of these quantities, and reasonably good for most of the remainder.

Special computer runs with a very fine mesh and small Courant number were made to define the limiting power-law behaviour of turbulence near a wall. Such behaviour was found to be confined to about 0.3 wall units from the wall, and to be: linear for streamwise turbulence, spanwise turbulence, vorticity normal to the wall, and for the departures from their respective wall values of dissipation, streamwise vorticity and spanwise vorticity; second power for turbulence normal to the wall; third power for Reynolds stress; and a constant value of the correlation coefficient for Reynolds stress. A simple physical explanation is given for the third-power variation of Reynolds stress and for the broad generality of this limiting variation.

Applications are made to Reynolds-average turbulence modelling: damping functions for Reynolds stress in eddy-viscosity models are derived that are compatible with the near-wall limiting behaviour; and new wall boundary conditions for dissipation in k - ϵ models are developed that are similarly compatible.

1. Introduction

The modelling of near-wall turbulence represents one of the weak links in present computational methods for wall-bounded flows. Turbulence production, dissipation and kinetic energy reach their maxima within the extremely thin viscous sublayer adjacent to a wall. Because of this thinness it has not been technically feasible to measure, in the variety of flows of practical interest, some of the important elements involved in turbulence modelling – such as dissipation rate and the limiting near-wall behaviour. Such circumstances have restricted significantly the accuracy of present turbulence models.

The objective of the present research is to explore use of the time-dependent Navier–Stokes equations as a method of modelling viscous sublayer turbulence, and thereby of investigating the limiting behaviour of turbulence very near a wall. This method attempts to model directly the experimental observations of highly elongate organized eddy structures near a wall. Such modelling is not limited by the extreme

thinness of the viscous sublayer, but is limited by the degree to which realism can be built into the boundary conditions for the Navier–Stokes equations.

One of the principal objectives of this research is to provide a basis for strengthening certain aspects of present Reynolds-average closure schemes. Because the modelled differential equations for free turbulence yield demonstrably incorrect results near a wall, various *ad hoc* functions (up to 5 in number for k - ϵ methods) are conventionally added in an effort to eliminate this shortcoming. Without a sound guide from experiment, the inevitable consequence has been that different models with different *ad hoc* functions have yielded different results (Patel, Rodi & Scheuerer 1981). Navier–Stokes computations can provide an improved guide to the modelling of these functions.

Another objective of this research is to use numerical computations to investigate the limiting behaviour of various turbulence quantities as the distance from the wall approaches zero. The limiting behaviour of Reynolds stress has long been a controversy (e.g. Hinze 1975). Some, for example, have suggested a third-power variation with distance from the wall, while others have suggested a fourth or even higher power. Numerical computations can define this behaviour by employing an extremely fine mesh near the wall.

The method used herein to model turbulence is termed ‘coherent-structure’ modelling, since it overtly attempts to model organized quasi-periodic eddy structures in the sublayer. In recent years several coherent-structure models of viscous sublayer turbulence have been explored. An initial model of Hatzivramidis & Hanratty (1979) used extremely simplified boundary conditions and obtained some interesting qualitative features, although the results were not quantitatively realistic in important respects (e.g. yielding zero Reynolds stress and zero turbulence intensity at the outer edge of the viscous sublayer). Subsequent coherent-structure models of Chapman & Kuhn (1981), Nikolaidis & Hanratty (1983), and Nikolaidis (1984) have employed somewhat more sophisticated boundary conditions in representing the coherent structures, and have yielded more realistic results. One unrealistic aspect of these models, however, is that they produce anomalously high values for dissipation near the outer edge of the viscous sublayer (Kaneda & Leslie 1982). Because dissipation is a key quantity modelled in Reynolds-average closure schemes, some attention was given in the present research to this anomaly, although it is not believed to affect the conclusions reached about the limiting behaviour of turbulence near a wall.

Three different coherent-structure models are explored herein. They differ mainly in the complexity of the space- and time-dependent boundary conditions imposed on the Navier–Stokes equations at the outer edge of the viscous sublayer. All of the models are restricted to incompressible flow without heat transfer. The mathematical development includes the effects of a mean streamwise pressure gradient, although comparisons with experimental data are made herein only for zero or small pressure gradients.

2. Experimental observations guiding model formulation

The key technical step in model development is to construct appropriate boundary conditions for the three fluctuating velocity components at the outer edge of the viscous sublayer (VSL). An attempt is made to formulate these so as to reflect as well as possible the main organized motions delineated by experiments. The principal observational features of coherent sublayer structure used as guidelines for the velocity boundary conditions to emulate are listed in the paragraphs which follow.

(i) Relatively small-scale eddies (SSE) produce the principal Reynolds stress through ejection and sweep motions (Kline *et al.* 1967; Corino & Brodkey 1969; Kim, Kline & Reynolds 1971; Wallace, Eckelmann & Brodkey 1972; Lu & Wilmarth 1973).

(ii) Organized large-scale eddies (LSE) are also observed (Kovasnay, Kibens & Blackwelder 1970; Falco 1977; Brown & Thomas 1977). Their mean period determined from streamwise autocorrelation data is $T_{LSE} \approx 5\delta/U_\infty$, independent of Reynolds number (Badri Narayanan & Marvin 1978).

(iii) Streamwise streaks of low-speed and high-speed fluid alternate spanwise (Kline *et al.* 1967; Gupta, Laufer & Kaplan 1971; Hirata *et al.* 1982; Moin & Kim 1982; Iritani, Kasagi & Hirata 1983). Many experiments indicate that the mean spanwise spacing between low-speed streaks is about $\lambda_+ \approx 100$.

(iv) Streamwise vortical motions are a prominent eddy structure at the outer edge of the VSL (Bakewell & Lumley 1967; Kline *et al.* 1967; Clark & Markland 1969; Kim *et al.* 1971; Lee, Eckelmann & Hanratty 1974; Willmarth 1975; Blackwelder & Eckelmann 1979; Kreplin & Eckelmann 1979; Kim 1983, 1984). The principal Reynolds-stress-producing events are associated with vortical pairs, although single streamwise vortical structures appear more common than pairs (Moser & Moin 1984).

(v) Coherent sublayer eddy structures are highly elongate streamwise, (Kline *et al.* 1967; Grass 1971; Kim *et al.* 1971; Cantwell, Coles & Dimotakis 1978; Blackwelder & Eckelmann 1979; Kreplin & Eckelmann 1979). Such observations enable a significant mathematical simplification to be made in the computational modelling.

(vi) There is a statistically mean period $\bar{T}_{B/\lambda}$ between ejection/sweep bursts per length λ of span when observed visually by the dye technique (Schraub & Kline 1965; Donohue, Tiederman & Reischman 1972; Smith 1978). There is also a different mean period \bar{T} between such bursts when measured by a hot wire at a fixed point in the flow. Various measurements of the latter show considerable scatter (e.g. Bandyopadhyay 1982) and vary with distance from the wall (Nakagawa & Nezu 1981). At the outer edge of the viscous sublayer, where our boundary conditions are applied ($y_+ = 40$), the recent measurements of Andreopoulos, Durst & Jovanovic (1983) and of Blackwelder & Haritonidis (1983) yield the relatively consistent result of $\bar{T}_+ \approx 250$ to 300 independent of Reynolds number.

(vii) The principal Reynolds-stress production is intermittent, consisting of periods of relative quiescence terminated by burst events (Corino & Brodkey 1969; Nychas, Hershey & Brodkey 1973; Offen & Kline 1975; Blackwelder & Kaplan 1976; Praturi & Brodkey 1978). Recent observations of Johansson & Alfredsson (1982) have also revealed large-scale inward motions (sweep) preceding an ejection event. Their data for the smallest threshold values and the longest integration times show ejection/sweep and sweep/ejection events to be about equally numerous. Hot-wire measurements indicate that the duration of these intensive events is only about 20–25% of the mean period between bursts.

(viii) Visual observations of the sublayer flow reveal it to be a mixture of order and disorder (Cantwell *et al.* 1978).

3. Computational models

Before describing features which distinguish between the three computational models, several features that are common to all are to be noted. These relate to the small-scale eddy structure, and to a mathematical approximation made in view of the highly elongate streamwise eddies observed in the viscous sublayer.

3.1. Common modelling characteristics

In each model, the boundary condition on each velocity component is composed of two separate components structured such that the Reynolds stress at the outer edge of the viscous sublayer is produced only by a small-scale eddy component (SSE, subscript 1) that is periodic in time and space. The SSE velocity boundary conditions are of the general form

$$u_{e1} = f(t) \sin \zeta, \quad v_{e1} = -f(t) \sin \zeta, \quad w_{e1} = f(t + \phi_{w1}) \cos \zeta, \quad (1)$$

where $\zeta = 2\pi Z/\lambda$ is the dimensionless spanwise coordinate, t is time, $f(t)$ is a periodic function with frequency N_1 , and ϕ_{w1} is a phase angle to allow for the circumstances that the spanwise velocity pulse in a burst may lead (or lag) the u_{e1} and v_{e1} components. All of these quantities are in dimensionless wall variables. This SSE structure corresponds to 180° phase difference between u_{e1} and v_{e1} , in accordance with experimental observations (Wallace, Brodkey & Eckelmann 1977) of conditionally sampled bursting events. The spanwise variation as $\sin \zeta$ for v_{e1} , and as $\cos \zeta$ for w_{e1} , correspond to a simple contrarotating vortical motion. The function $f(t)$ is structured such that for $0 < \zeta < \pi$ an ejection precedes a sweep, whereas for $\pi < \zeta < 2\pi$ a sweep precedes an ejection. Thus ejection/sweep and sweep/ejection events are equally numerous in the models.

The mean frequency N_1 of the SSE burst events is also taken to be the same for all models. With the variable-interval time average (VITA) technique used by Blackwelder & Haritonidis (1983) to determine bursting frequency, only ejection/sweep events were counted. Since these meander spanwise over a fixed hot-wire probe, their measured mean frequency of $\bar{f}_{es} \approx 0.0035$ wall units would correspond to an average over space and time in the computational models. For $0 < \zeta < \pi$ the frequency of computational ejection/sweep events is $\frac{1}{2}N_1\pi$. For $\pi < \zeta < 2\pi$ it is 0. Thus the average frequency of ejection/sweep events over space and time is $\bar{f}_{es} = N_1/4\pi$, which corresponds to the value $N_1 = 4\pi(0.0035) = 0.044$.

This value for N_1 is not inconsistent with the mean burst period of $\bar{T}_{B/\lambda} \approx 120$ determined from visual observations with the dye technique (Schraub & Kline 1965; Donohue *et al.* 1972; Smith 1978). If an ejection precedes a sweep, dye first accumulates along the spanwise station of the event and then becomes visible as a burst of dye when it is subsequently ejected upward. If a sweep precedes an ejection, however, dye is first removed away from the spanwise station of the event by the sweep; and hence there may not be enough dye left at this station to make the subsequent ejection visible. Thus the 'burst' frequency per λ of span from dye visualization may represent primarily the mean frequency of ejection/sweep events, while missing most of the sweep/ejection events. If this is the case, then the dye technique would yield $\bar{T}_{es/\lambda} \approx 120$. In the computational model $N_1\bar{T}_{es/\lambda} = 2\pi$, so that the value of $N_1 = 0.044$ corresponds to $\bar{T}_{es/\lambda} = 143$, reasonably close to the value interpreted from dye observations.

Still further elements of commonality for all models are the turbulence intensities at the outer edge of the viscous sublayer. These are inputs α , β , γ into the computations defined in wall variables as

$$\alpha = \langle u_{e+}^2 \rangle, \quad \beta = \langle v_{e+}^2 \rangle, \quad \gamma = \langle w_{e+}^2 \rangle, \quad (2)$$

for streamwise, normal and spanwise turbulence intensities respectively. The values $\alpha = 2$, $\beta = 1$ and $\gamma = 1.3$ are used throughout.

The conventional wall variables used herein are defined as

$$\left. \begin{aligned} u_\tau^2 &= \frac{\tau_w}{\rho}, & T &= \frac{tu_\tau^2}{\nu}, & P &= \frac{p}{\tau_w} = \frac{\bar{p} + \Delta p}{\tau_w}, \\ X &= \frac{xu_\tau}{\nu}, & Y &= y_+ = \frac{yu_\tau}{\nu}, & Z &= \frac{zu_\tau}{\nu}, \\ U = u_+ &= \frac{u}{u_\tau}, & V = v_+ &= \frac{v}{u_\tau}, & W = w_+ &= \frac{w}{u_\tau}, \\ N &= \frac{\nu}{u_\tau^2}. \end{aligned} \right\} \quad (3)$$

The experimental observation of highly elongate streamwise eddies in the viscous sublayer provides a basis for mathematically simplifying the models. Velocity derivatives in the streamwise direction are neglected compared with velocity derivatives in the spanwise and normal directions. The recent turbulence simulations of Moser & Moin (1984) show that, although the u -patterns are elongate streamwise, the v - and w -patterns are less so; hence some approximation is introduced by making this mathematical simplification. The approximation treats three velocity components fluctuating in two space dimensions and time (Y, Z, T).† Being more than two-dimensional flow, but not fully three-dimensional, this mathematical approximation has been termed ‘two-and-a-half-dimensional’ flow, or ‘slender-turbulence’ theory.

3.2. Three models investigated

The three different computational models investigated are distinguished mainly by their outer-edge boundary conditions on velocity. The models are termed Model 1, 2 and 3 in order of increasing complexity.

Model 1

This relatively simple model is essentially the same as that reported by Chapman & Kuhn (1981). It considers two coherent harmonic components of motion at the outer edge: one represents small-scale eddies (SSE) and the other large-scale eddies (LSE). The three fluctuating edge velocities are:

Component 1	Component 2	
SSE	SSE	
$\left. \begin{aligned} u_e &= 2\alpha_1 \sin(N_1 T) \sin \zeta \\ v_e &= -2\beta \sin(N_1 T) \sin \zeta, \\ w_e &= 2\beta \sin(N_1 T + \phi_w) \cos \zeta \end{aligned} \right\}$	$\left. \begin{aligned} &+ [2(\alpha^2 - \alpha_1^2)]^{\frac{1}{2}} \sin(N_{u_2} T + \phi_{u_2}), \\ &+ [2(\gamma^2 - \beta^2)]^{\frac{1}{2}} \sin(\frac{1}{2} N_{u_2} T + \phi_{w_2}). \end{aligned} \right\}$	(4)

In order for the $(uv)_e$ correlation coefficient to be 0.45, α_1/α also must be 0.45; and hence $\alpha_1 = 0.9$. In order for $(d\bar{v}^2/dY)_e$ to be zero in accordance with experimental data, it follows from the continuity equation that $\phi_{w_1} = \frac{1}{2}\pi$. The value $\phi_{w_2} = \frac{2}{3}\pi$ is determined by computer trial to yield as good agreement as possible with the law of the wall for $\langle U(Y) \rangle$, the slope at the wall, and the Reynolds-stress distribution. The value $\phi_{u_2} = 0$ is also determined by computer trial to yield a reasonable level of skewness for u_e . Since N_1 is taken as 0.044, the computations for model 1 differ

† Inasmuch as we use wall variables throughout, the + subscript will be dropped from velocity components and coordinates for simplicity in the remaining sections of this text.

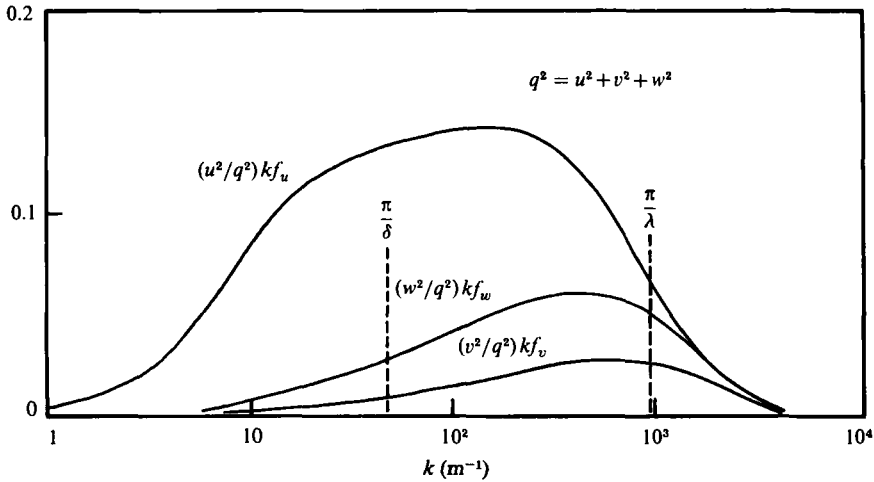


FIGURE 1. Spectral density of the three components of velocity fluctuation at $Y = 40$ from data of Fulachier (1972).

somewhat from those of Chapman & Kuhn who used $N_1 = 0.025$, $\phi_{w2} = \frac{3}{4}\pi$ and $\phi_{u2} = \frac{1}{3}\pi$, but otherwise used the same constants.

The LSE frequency N_{u2} is determined by the mean period \bar{T}_{LSE} of organized large-scale eddies as obtained from the experimental relationship $U_\infty \bar{T}_{LSE} \approx 5\delta$. Since $N_{u2} \bar{T}_{LSE} = 2\pi$, the large-eddy frequency is $N_{u2} = 2\pi U_\infty / 5\delta$, which is Reynolds-number-dependent. For simplicity, numerical computations herein have been made for $N_{u2} = N_1 = 0.044$. This corresponds to a Reynolds number of $Re_\delta \approx 14000$ for a plate or channel flow. By making computations at this Reynolds number at which outer and inner frequencies are equal, we circumvent the issue of whether the large-scale eddies scale with outer variables or wall variables.

Model 2

Relative to Model 1, Model 2 adds complexity by structuring the velocity boundary conditions to simulate intermittent production of burst events and hence of Reynolds stress. Also, two components of velocity for each of u_e , v_e and w_e were modelled to represent the principal eddy scales reflected in spectral data. Such data for all three velocity components have been obtained by Fulachier (1972) at y -values near the outer edge of the viscous sublayer. Spectral parameters at $Y = 40$, interpolated between his measurements at $Y = 31$ and 77 , are shown in figure 1 wherein k represents the wavenumber determined by the Taylor hypothesis and the mean streamwise velocity, and f the spectral density. The areas under the curves of $u^2 kf_u$, $v^2 kf_v$ and $w^2 kf_w$ versus $\log(k)$ are proportional to the relative amounts of kinetic energy in these velocity components. The two dashed lines shown along the k -axis correspond to large eddies of scale π/δ (where δ is the boundary-layer thickness) and to the small eddies of scale π/λ .

The use of these streamwise spectral data to provide model information for the spanwise validation of u , v and w is based on identification of the small-scale eddies with the elongated structures, as in Model 1. The intermediate- and large-scale eddies are then assumed to be identified as having longer spanwise wavelengths. The Reynolds-stress-producing SSE, of course, must be included for all three velocity components. If only a second component is selected, the spectral data suggest that the most appropriate such component would be a large-scale eddy for u , and

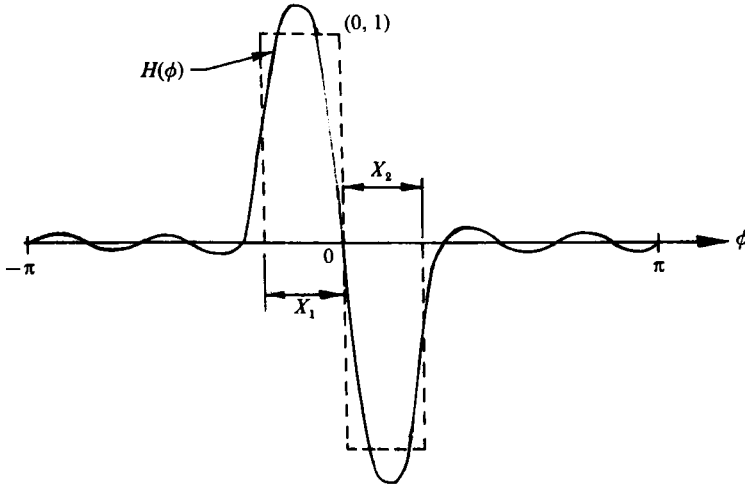


FIGURE 2. Sketch of truncated Fourier series approximation to rectangular pulse function.

medium-scale eddies (MSE) for v and w . In contradistinction to the structure of Model 1, these spectral data do not indicate the presence of a major LSE component for w . Thus the boundary conditions for Model 2 are structured to represent SSE and LSE for u_e , coupled with SSE and MSE for v_e and w_e . The latter MSE are structured to be out of phase in both space and time in order to yield $\overline{uw} = 0$ throughout the sublayer.

SSE	LSE	MSE	
Scale λ	Scale $< 10 \lambda$	Scale 3λ	
$u_e = \sqrt{2} \alpha_1 F_u(\phi) \sin \zeta$	$+ \sqrt{2} \alpha_2 \sin(N_{u2}T + \phi_{u2}),$	$+ 2\beta_3 \sin(N_{v3}T) \sin \frac{1}{3} \zeta,$	} (5)
$v_e = -\sqrt{2} \beta_1 F_v(\phi) \sin \zeta$		$+ 2\gamma_3 \cos(N_{w3}T) \cos \frac{1}{3} \zeta,$	
$w_e = \sqrt{2} \gamma_1 F_w(\phi) \cos \zeta$			

where T = time in wall variables, and N_1 = frequency of ejection/sweep events, $N_{u2} = 2\pi U_\infty / 5\delta$ = frequency of large-scale eddies, $N_{v3} = N_{w3}$ = frequency of medium-scale eddies, $\zeta = 2\pi Z / \lambda$, $\phi = N_1 T$,

$$-F_u(\phi) = F_v(\phi) = \frac{H(\phi)}{[H^2(\phi)]^{\frac{1}{2}}}, \tag{6}$$

$$F_w(\phi) = -\frac{H(\phi + \phi_{w1})}{[H^2(\phi + \phi_{w1})]^{\frac{1}{2}}}. \tag{7}$$

The function $H(\phi)$ is formed by the first M terms of a Fourier series approximating the intermittent rectangular pulse function sketched in figure 2.

$$H(\phi) = \sum_1^M [a_n \cos(n\phi) + b_n \sin(n\phi)], \tag{8}$$

$$\overline{H^2(\phi)} = \frac{1}{2} \sum_1^M (a_n^2 + b_n^2), \tag{9}$$

$$a_n = \frac{1}{\pi n} \left[\sin(nX_1) - \frac{X_1}{X_2} \sin(nX_2) \right], \tag{10}$$

$$b_n = \frac{1}{\pi n} \left\{ \frac{X_1}{X_2} [\cos(nX_2) - 1] + [\cos(nX_1) - 1] \right\}. \tag{11}$$

Values of M between 3 and 5, and values of $X_1 \neq X_2$ have been investigated with little difference in computed results. For the results presented herein, $M = 5$ and $X_1 = X_2 = 0.3$. The phase angle $\phi_{u_2} = 60^\circ$ was determined by computer trial, as in Model 1, to yield a reasonable level for the skewness of u . The phase angle $\phi_{w_1} = 25.8^\circ$ was mathematically determined, also as in Model 1, by the requirement that $(\partial v^2 / \partial y)_e = 0$. Since $M = 5$, this particular determination involved solving for the roots of a fifth-order polynomial. It is noted that $\phi_{w_1} = 25.8^\circ$ corresponds to the SSE pulse in w leading in time the corresponding ejection/sweep pulses of u and v .

The $(uv)_e$ correlation coefficient for the above boundary conditions is $-(R_{uv})_e = \alpha_1 \beta_1 / \alpha \beta$, which is set equal to 0.45. The ratio β_1 / β is evaluated from various experimental data on peak-to-peak amplitude ratios in ejection/sweep events (Kim *et al.* 1971; Blackwelder & Kaplan 1976; Chen & Blackwelder 1978; Nakagawa & Nezu 1981). Such data suggest a value of β_1 / β between 0.49 and 0.72. For simplicity, $\beta_1 / \beta = 1/\sqrt{2} = 0.707$ is used in the numerical computations. This corresponds to equal amounts of v^2 energy in small-scale and medium-scale eddies. From the correlation-coefficient equation it follows that $\alpha_1 / \alpha = 0.635$.

The value of γ_1 / γ was determined by computer trial to yield a relatively smooth curve for $w'(Y)$. In runs with only the SSE active, it was found that various prescribed values of γ_1 would result in substantially the same level of $(w') \approx 0.45$ over much of the sublayer. Hence, $\gamma_1 = 0.45$ was selected as the outer-edge turbulence intensity of the SSE for Model 2.

The frequency N_{u_2} of the large-scale eddies is taken to be the same as for Model 1. As in Model 1, numerical computations for Model 2 have been made for $N_{u_2} = N_1 = 0.044$, corresponding to a Reynolds number of $Re_\delta \approx 14000$. The frequencies N_{v_3} and N_{w_3} were taken to be equal. In the calculations for Model 2 they were taken to be $N_{v_3} = N_{w_3} = 3N_1$. This choice was based on the assumption that the small scales are the highly elongate structures which persist for some time, while the large scales are more transient. Thus, it is reasonable to take the large-scale or intermediate-scale frequency to be greater than that of the small scales. Also, the small scales are intermittent so that the relation between N_1 and N_{v_3} and N_{w_3} is not really 1 to 3, but more like 4 to 3. The ultimate choice was based on the results of numerical experiments which indicated that $N_{v_3} = N_{w_3} = 3N_1$ was the best.

For Model 2 a body pressure gradient is not imposed in association with the large-scale eddies. This feature differs from Model 1. Computer runs for Model 2 were made both with and without the body pressure-gradient term. The results were somewhat better without this term, although the differences were not major.

In summary thus far, Model 2 differs from Model 1 in several ways: it simulates intermittent bursting and Reynolds-stress production, rather than sinusoidal as in Model 1; it employs a medium-scale eddy component for v_e , whereas Model 1 has none; and it also employs a medium-scale component for w_e , whereas Model 1 employs a large-scale component. A further difference is that Model 2 does not employ a body pressure-gradient term associated with the large-scale eddy component for u .

Model 3

The primary feature characterizing Model 3 is the use of time functions for LSE and MSE that are randomly generated instead of harmonic. Otherwise it is similar to Model 2. The periodic small-scale eddy structure remains the same as in Model 2.

The outer-edge boundary conditions for Model 3 are

SSE	LSE	MSE	
Scale λ	Scale $\geq 10 \lambda$	Scale 3λ	
$u_e = \sqrt{2} \alpha_1 F_u(N_1 T) \sin \zeta + \alpha_2 R_{u_2}(T),$			(12)
$v_e = \sqrt{2} \beta_1 F_v(N_1 T) \sin \zeta$		$+ \sqrt{2} \beta_3 R_{v_3}(T) \sin \frac{1}{3} \zeta,$	
$w_e = \sqrt{2} \gamma_1 F_w(N_1 T) \cos \zeta$		$+ \sqrt{2} \gamma_3 R_{w_3}(T) \cos \frac{1}{3} \zeta,$	

where the three functions $R_{u_2}(T)$, $R_{v_3}(T)$, $R_{w_3}(T)$ are random functions of time, each independently generated, and each normalized to have an r.m.s. value of unity. All constants N_1 , α_1 , α_2 , β_1 , β_3 , γ_1 and γ_3 are the same as in Model 2. Model 3 simulates disorder in the LSE and MSE, whereas Model 2 simulates relatively coherent harmonic order in these eddies.

4. Numerical computation method

A computer code recently developed by Kim & Moin (1984) was adapted to the conditions of this study. The reader is referred to their report for details of the numerical algorithms. A brief qualitative description is given herein of the numerical method along with an account of the modification made for present computations.

With the pressure gradient split into three terms, the Navier–Stokes equations in tensor notation are

$$\frac{\partial U_i}{\partial t} = -\frac{\partial}{\partial x_j} (U_i U_j) - \frac{\partial P}{\partial x_i} - \frac{\partial \bar{P}}{\partial x_i} + F_i(T) + \nabla^2 U_i, \tag{13}$$

$$\frac{\partial U_i}{\partial x_i} = 0 \quad (i = 1, 2, 3), \tag{14}$$

where U_i = the velocity components U , V , W corresponding to $i = 1, 2, 3$ (streamwise, normal, spanwise) respectively, \bar{P} is the mean pressure normalized by the wall shear stress τ_w , P is the pressure perturbation normalized by the wall shear stress, F_i is a body force used in Model 1 which corresponds to a global pressure gradient associated with the LSE, and x_i is the Cartesian coordinates X , Y , Z in wall variables.

The equations are to be solved in a rectangular region $0 \leq Y \leq Y_e$, $0 \leq Z \leq Z_{\max}$. The flow is assumed to be periodic in Z with zero velocity at $Y = 0$. At $Y = Y_e$, the boundary conditions are

$$U_i(X, Y_e, Z) = (U_i)_{e1}(Z, T) + (U_i)_{e2}(T). \tag{15}$$

In Model 1, the functions $F_i(T)$ are taken to correspond to the LSE pressure gradients of simple oscillating shear flow in the X - and Z -directions. Thus, for this model

$$F_1(T) = \frac{\partial (U_1)_{e2}}{\partial T} = \frac{\partial u_{e2}}{\partial T}, \tag{16}$$

$$F_2(T) = 0, \tag{17}$$

$$F_3(T) = \frac{\partial (U_3)_{e2}}{\partial T} = \frac{\partial w_{e2}}{\partial T}, \tag{18}$$

and the mean pressure \bar{P} is assumed to be a function of X alone. For Models 2 and 3, $F_i(T)$ was set to zero.

For numerical solution of (13) and (14), Kim & Moin use an Adams–Bashforth

formula for convective terms, and centred differences for viscous terms. A factored semi-implicit solution algorithm is used that is explicit in convective terms, and implicit in viscous terms. The first step in time-advancing the solution calculates a predictor velocity field which satisfies appropriate boundary conditions, but not the continuity equation. A second step then corrects the velocity field to satisfy the continuity equation and the Poisson equation for pressure. The method is second-order accurate in both space and time.

An accuracy test of the Kim-Moin code was made by computing oscillating shear flow and comparing results with exact analytical solutions (Chapman & Kuhn 1981). With 320 time steps per cycle, and 17 points uniformly spaced across the oscillating layer, the numerical method was found to be very accurate, reproducing the analytical solution within 0.1 %.

In making numerical computations, an arbitrary initial velocity profile is needed at $T = 0$. To accelerate convergence to periodicity, an analytical approximation for a turbulent-boundary-layer profile was used. The boundary conditions at Y_e were multiplied by a factor which starts at zero and reaches unity asymptotically over the first time cycle of the computation. The solution was then advanced until periodic flow conditions were attained, usually after about 3 or 4 cycles of time for Models 1 and 2. Space and time averages were then taken over a cycle of periodic flow. A typical computation of viscous-sublayer turbulence for our normal mesh used 400 time steps per small-scale cycle: 30 points in the Y -direction; 32 points in the Z -direction; and, for Models 1 and 2, required 4 to 5 minutes of CRAY X-MP time per run. The corresponding run time for Model 3 was considerably longer due to the lack of periodicity. For the special fine mesh used to define the near-wall behaviour of turbulence, up to 3200 time steps per small-scale cycle were used with 60 points in the Y -direction, 64 in the Z -direction, and a run time of over one hour.

The computational method was found to be quite stable as long as the time step was smaller than a certain value which depends on the spatial grid size. The particular value was determined by trial and error for each grid. Below the instability limit, the solution obtained was not strongly dependent upon the time-step size, but was affected somewhat by the spatial grid.

The method used to generate random time sequences for Model 3 is given in Chapman & Kuhn (1984). In order to keep computer time within acceptable bounds the correlation coefficient between two successive terms in a time sequence was set at 0.95. This corresponds to an integral time-scale of approximately 40 wall units, close to the experimental value for the u -component as deduced from the data of Fulachier (1972) and Elena (1977).

In order to obtain relevant results for the statistical quantities, the random sequences must be calculated until a steady state is reached. The number of steps required for this is not known *a priori*. Owing to the combination of periodic and random functions, the total number of steps used must be an integral number of periods of the small-scale components. For the results discussed herein, the calculations were carried out until two successive cycles resulted in a negligible change in the accumulated statistics.

5. Computational results compared with experiment

Law of the wall. As illustrated in figure 3, the mean streamwise velocity profile computed for Models 1 and 2 agrees well with experiment. For Model 3, however, the computed values of $\langle U \rangle$ are low. Because of the relatively long computer times

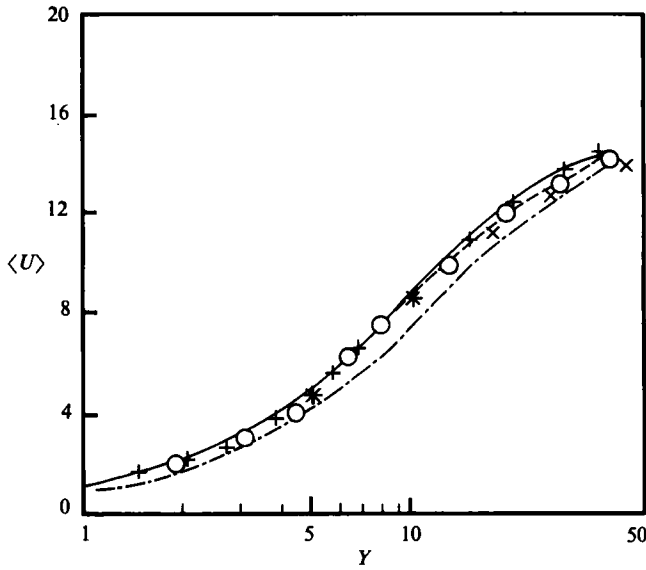


FIGURE 3. Mean streamwise velocity profiles: —, Model 1; --, Model 2; - · - ·, Model 3; ○, Hussain & Reynolds (1975); ×, Laufer (1954); +, Ueda & Hinze (1975).

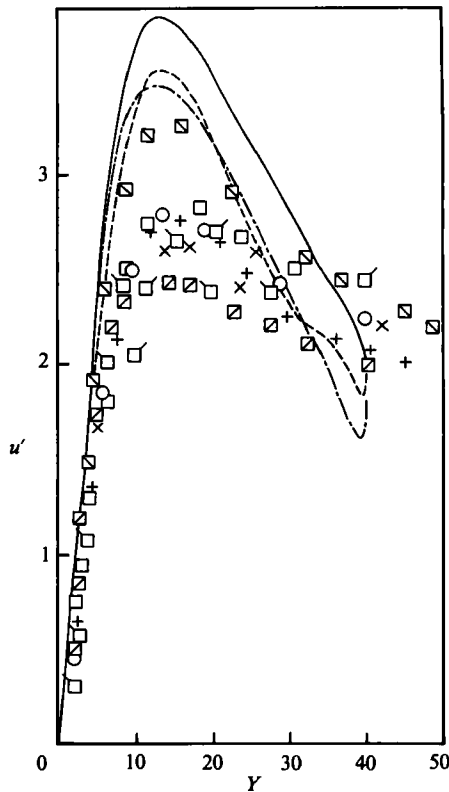


FIGURE 4. Intensity of streamwise velocity fluctuations. ○, Schildknecht, Miller & Meier (1979); □, □, Kutateladze *et al.* (1977); ◻, Clark (1968); +, Ueda & Hinze (1975); ◻, Laufer, (1950); ◻, Hussain & Reynolds (1975); ×, Laufer (1954); —, Model 1; --, Model 2; - · - ·, Model 3.

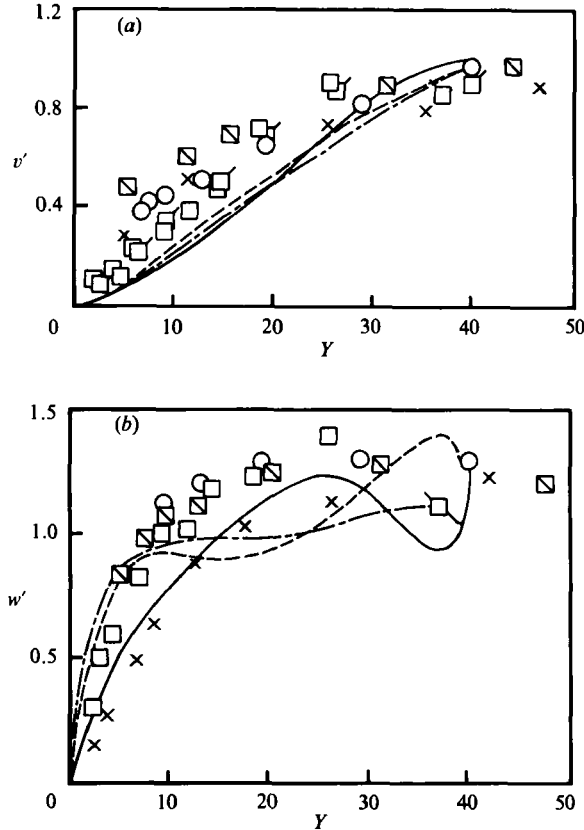


FIGURE 5. Intensity of normal and spanwise turbulence. Legend as in figure 4. (a) v' , (b) w' .

required when random time functions are used, systematic variations in the parameters of Model 3 were not explored. It is possible, therefore, that modest changes in these parameters could bring the computed $\langle U \rangle$ profiles for Model 3 into agreement with experiment comparable to that of Models 1 and 2.

Intensity of turbulence. The computed r.m.s. intensity of streamwise turbulence u' is not greatly different for the three models (figure 4). Each model yields peak values of u' higher than experiment. For models 2 and 3 some irregularities can be seen near the outer edge of the viscous sublayer (Y between about 35 and 40). This irregularity, as shown later, is manifested in a more pronounced outer-edge anomaly in the rate of dissipation and the intensity of streamwise vorticity fluctuations. The slope of the curve of $u'(Y)$ at $Y=0$ is equal to $S'_x = \langle (\tau_{xw} - \langle \tau_{xw} \rangle)^2 \rangle^{1/2} / \langle \tau_w \rangle$, the fluctuating intensity of streamwise wall shear stress. In wall units, computed values of S'_x for the normal mesh are 0.55, 0.47 and 0.50 for Models 1, 2 and 3 respectively. These values are higher than experimental values, which range between 0.24 and 0.49. Runs with finer mesh intervals did not change appreciably the computed values of S'_x .

The computed intensity of turbulence v' normal to the wall is nearly the same for all three computational models (figure 5a). Although experiments indicate higher values of v' near the wall, this may be due in sizeable part to experimental errors, since hot-wire measurements of v' are notoriously inaccurate near a wall. Most of the experimental data, in fact, extrapolate erroneously to non-zero values at the wall.

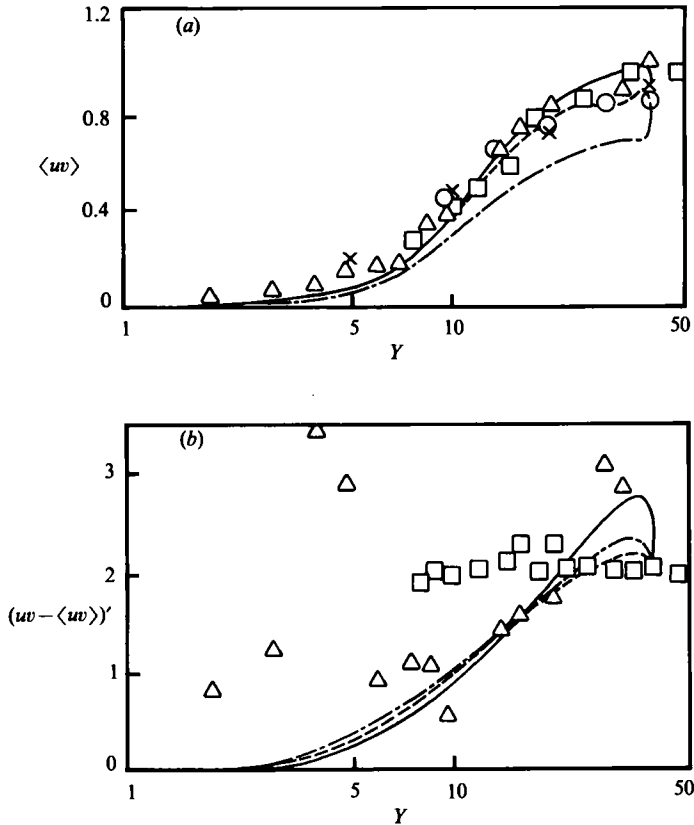


FIGURE 6. Mean Reynolds stress and intensity of Reynolds-stress fluctuations. \circ , Schildknecht *et al.* (1979); \triangle , \square , Gupta & Kaplan (1972), \times , Laufer (1954); —, Model 1; ---, Model 2; - · - ·, Model 3. (a) Reynolds stress. (b) Intensity of Reynolds-stress fluctuations.

The computational curves of spanwise turbulence intensity w' (figure 5*b*) show more variation between the three models. Although the computed levels of w' are in reasonably good agreement with experiment for all three models, some irregularity is again exhibited near the outer edge. At the wall, the slopes of the w' curves, representing the intensity of spanwise shear-stress fluctuations, are 0.14 and 0.31 for Models 1 and 2 respectively. These values were determined from runs with a fine mesh. Experimental values are about 0.1.

Reynolds stress. The computed distributions of $\langle uv \rangle$, as might be expected, show similar results to those for $\langle U(Y) \rangle$. This is illustrated in figure 6(*a*). For Models 1 and 2 the Reynolds-stress computations agree very well with experiment, but for Model 3 the computed values are low. In the case of Model 1 the parameters ϕ_{w2} and ϕ_{u2} were determined by computer trial to provide good agreement with Reynolds-stress measurements; and in the case of Model 2, the parameters ϕ_{w3} and ϕ_{u2} were determined likewise; but for Model 3 these parameters do not appear. The parameters β_1 and γ_1 , however, were found in Models 1 and 2 to affect $\langle uv \rangle$ and $\langle U(y) \rangle$. Primarily because of the long computer times required for Model 3, however, such parameter adjustments were not investigated.

The computed r.m.s. fluctuations in Reynolds stress as shown in figure 6(*b*) also differ relatively little between the three models. Considering that the experimental

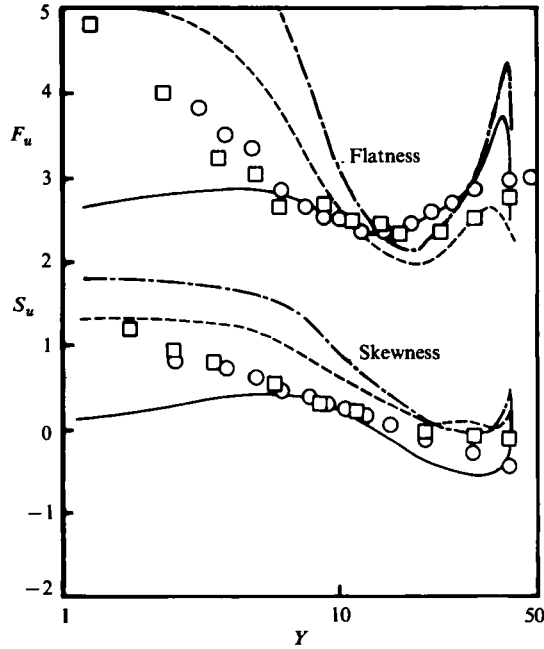


FIGURE 7. Skewness and flatness of u velocity fluctuations. \circ , Ueda & Hinze (1975); \square , Elena, Fulachier & Dumas (1979); —, Model 1; ---, Model 2; - · - ·, Model 3.

data scatter widely – because of the inherent difficulty of such measurements very near a wall – the agreement between computation and experiment is reasonably good.

It is also noted that in the outer region of the viscous sublayer, the r.m.s. fluctuations in uv are about twice the mean value \overline{uv} , for both computation and experiment.

Skewness and flatness factor. Distributions of skewness and flatness factor for the streamwise velocity fluctuations are presented in figure 7. Near the wall, both skewness and flatness are low for Model 1 with its simple harmonic boundary conditions on velocity. For Model 2, which simulates more realistically the intermittent character of burst events, these factors are in much better agreement with experiment near the wall, as might be expected. In the case of Model 3 with randomly generated time functions, the skewness and flatness of u' are considerably greater than for Model 2 and the experimental data. The reason for this is uncertain. A possible cause may be that these higher-order statistics may require larger computation times to reach steady conditions than do the lower-order statistics such as u' , v' , etc.

Similar characteristics are exhibited by the skewness and flatness factor for the fluctuating Reynolds stress (figures 8*a*, *b*). Here again, the flatness factor for Model 2 agrees better with experiment than does Model 1. Computations were not made of the Reynolds-stress skewness and flatness for Model 3.

Correlation coefficient R_{uv} . As shown in figure 9, all three models yield values of R_{uv} of between about 0.4 and 0.5 in the outer three-quarters of the viscous sublayer. The computations for Models 3 and 2 exhibit very similar trends, indicating that the use of random time functions in place of periodic ones has only a small effect on the u - v correlation. Experimental data scatter widely below Y of about 10, with one data

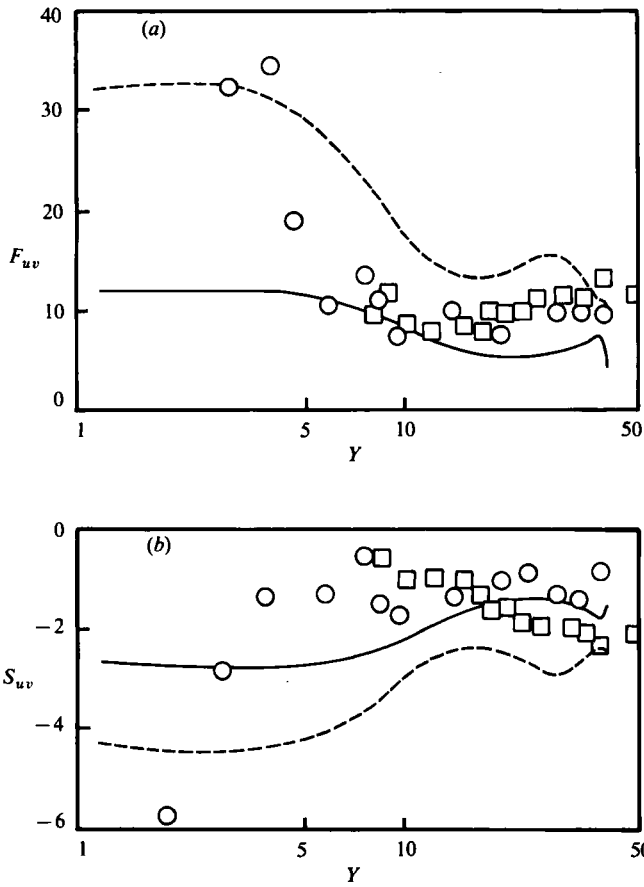


FIGURE 8. Skewness and flatness of Reynolds-stress fluctuations. \circ , \square , Gupta & Kaplan (1972); —, Model 1; --, Model 2. (a) Flatness. (b) Skewness.

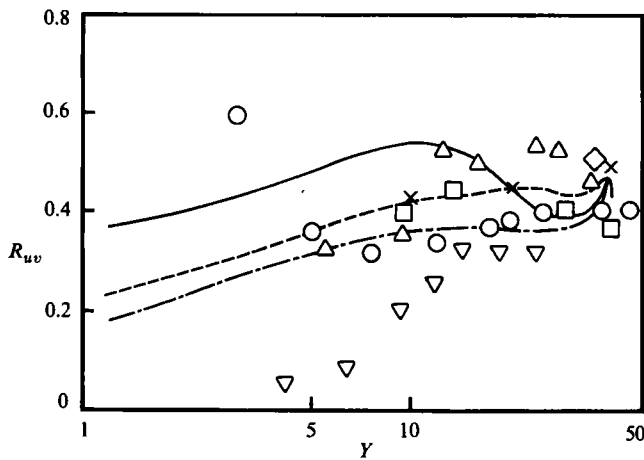


FIGURE 9. Reynolds-stress correlation coefficient. \circ , Eckelmann (1974); \triangle , Kim *et al.* (1971); \square , Schildknecht *et al.* (1979); ∇ , Kutateladze *et al.* (1977); \diamond , Laufer (1950); \times , Laufer (1954); —, Model 1; --, Model 2; - · - ·, Model 3.

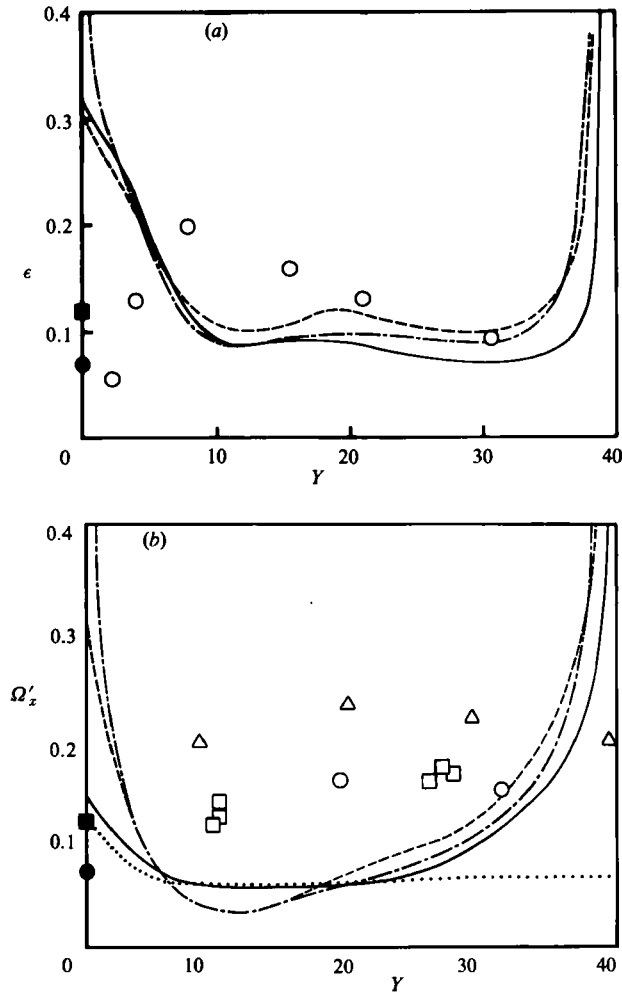


FIGURE 10. (a) Turbulence dissipation; \circ , Laufer (1954); \bullet , Kreplin & Eckelmann (1979); \blacksquare , Hogenes & Hanratty (1982); —, Model 1; ---, Model 2; - · - ·, Model 3. (b) Streamwise vorticity fluctuations: \circ , Kastrinakas & Eckelmann (1983); \square , Kasagi *et al.* (1984); \triangle , Kastrinakas *et al.* (1975); \bullet , Kreplin & Eckelmann (1979), \blacksquare , Hogenes & Hanratty (1982); \dots , Moin & Kim (1982).

set (Eckelmann 1974) suggesting increasing values of R_{uv} as the wall is approached, whereas another set (Kutateladze *et al.* 1977) indicates strongly decreasing values. Considering the wide scatter of these experimental data, all three models yield apparently acceptable computations of R_{uv} .

Dissipation and streamwise vorticity fluctuation. These two quantities illustrated in figure 10 reveal most clearly the existence of an anomaly in all three models near the outer edge of the viscous sublayer. Both the rate of turbulence dissipation ϵ , and the r.m.s. intensity of fluctuating streamwise vorticity Ω'_x , exhibit anomalously high values in the outer region between about $Y = 35$ and $Y = 40$. Since ϵ and Ω'_x reflect the magnitude of velocity gradients, it is clear that all three models produce a region near the outer edge in which velocity gradients are large and vary rapidly with Y . Such a region is of the Stokes-layer type. It is believed to be due to some unrealistic aspect of the velocity boundary conditions imposed at $Y = 40$, to which the

Navier–Stokes equations make rapid adjustment, leaving most of the turbulence characteristics below Y of about 35 in reasonable accord with reality.

Inasmuch as dissipation rate is a quantity often used in Reynolds-average modelling to determine the important length scale of turbulence, an effort was undertaken to vary the model parameters and eliminate, if possible, this undesirable anomaly. Systematic variations were made in the parameters $\alpha_1, \beta_1, \gamma_1, N_1, N_2, N_{w3}, \phi_{w1}, \phi_{u2}, \phi_{w3}, \lambda, X, M,$ and $(Y)_e$. While some changed the value of ϵ at the outer edge, none eliminated or reduced it by more than a factor of about 2. In addition, phase angles in spanwise space and time for the intermediate-scale component of Model 2 were introduced and varied, but without any essential effect on the anomaly. Moreover, the spanwise profiles of velocity were altered from $\sin \zeta$ to $\sin^p \zeta$, with p being a power greater or less than one, and still the anomaly remained. When runs were made with only the small-scale eddy components present, and without any large- or intermediate-scale components, it was found that the anomaly still existed. On the other hand, it was not present when only the large-scale components of velocity were used. The large-scale components contain only a time-varying term and that only in the u - and w -velocity components. We conclude, therefore, that the outer-edge anomaly is a consequence of some unrealistic aspect in the structure of the velocity boundary conditions for the small-scale eddies which produce the Reynolds stress in all three models.

It may be noted that the Stokes-layer anomaly at the outer edge is not attributed to the approximation of two-and-a-half-dimensional flow. In principle, the velocity fields computed at Y of 30, say, could have been used as outer-edge boundary conditions imposed at $Y_e = 30$, and identical results would have been produced below Y of 30 without an anomaly. A cursory examination of the velocity fields at $Y = 30$ showed them to be much more complex than the conditions imposed at Y_e . More detailed study of such fields might provide a guide as to how the small-scale-eddy velocity components could properly be constructed without producing an anomaly at the outer edge.

6. Near-wall limiting behaviour of turbulence

Although experimental techniques to date have been unable to determine the limiting behaviour of turbulence very near a wall, several different ideas have been advanced. Over thirty years ago, Reichardt (1951) concluded that for streamwise inhomogeneous flows, u' would be proportional to y , v' to y^2 , and \overline{uv} to y^3 , as y approaches zero, but that for streamwise homogenous flows \overline{uv} would be proportional to y^4 . Elrod (1957) arrived at the same conclusion. The widely used and highly successful damping-factor model of eddy viscosity by Van Driest (1956) corresponds also to $\overline{uv} \sim y^4$ near a wall. Some support for this appeared to be provided by the theoretical results of Ohji (1967) for homogenous flows which also yielded near the wall $\overline{uv} \sim y^4$, together with $R_{uv} \sim y$ and $(R_{uv})_w = 0$. On the other hand, Coles (1985) has recently obtained $\overline{uv} \sim y^3$ for a simple contrarotating vortex model of viscous-sublayer flow. Reviews of differing views on the y^3 versus y^4 controversy have been given by Hinze (1975), and by Monin & Yaglom (1971).

Numerical computations from the Navier–Stokes equations offer a means of resolving this issue. Towards this end, computations with very fine meshes and small Courant numbers have been made for Models 1 and 2 for the case of zero pressure gradient. (Considerations of computer time precluded doing this for Model 3.) In the y -direction 60 points were used across the viscous sublayer, with clustering near the

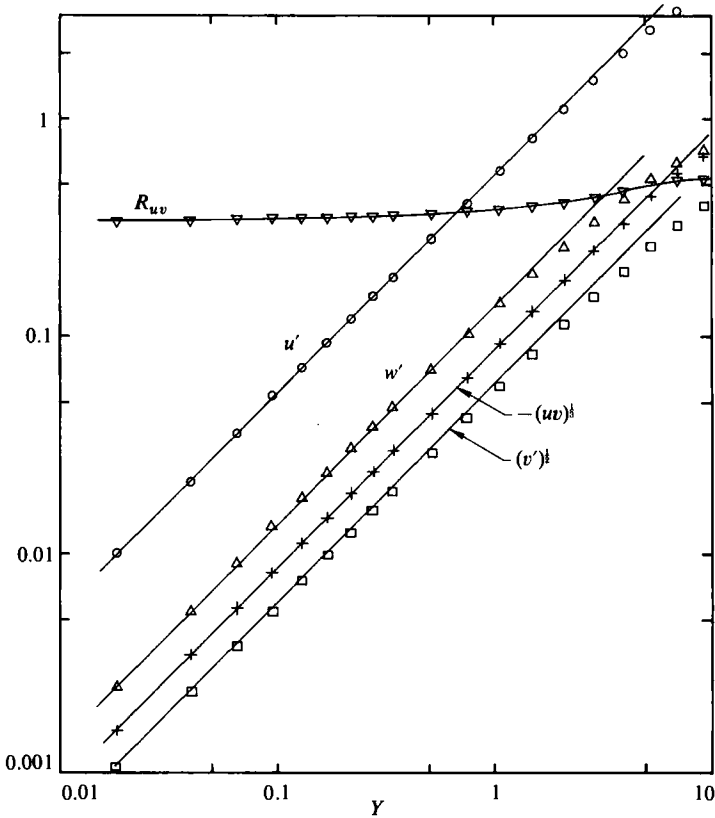


FIGURE 11. Near-wall behaviour of turbulence for Model 1: \circ , u' ; \square , $(v')^{1/2}$; \triangle , w' ; ∇ , R_{uv} ; $+$, $-(uv)^{1/2}$. Inclined straight lines are proportional to Y .

wall and with the closest point at $Y = 0.018$. In the z -direction 64 points were used evenly spaced spanwise. Owing presumably to a numerical truncation error at the wall boundary, the wall turbulence values were not precisely zero (ranging from 10^{-12} for $\langle uv \rangle$ to 10^{-4} for w') and were subtracted out in order for the turbulence to be precisely zero at the wall. The results are shown as log-log plots in figures 11 and 12 for the range of Y between 0.01 and 10. Inclined straight lines in these figures are proportional to Y . The limiting near-wall behaviour in each model is clearly $u' \sim y$, $v' \sim y^2$, $w' \sim y$, $\langle uv \rangle \sim y^3$, and $(R_{uv})_w = \text{constant} \neq 0$. The constants of proportionality, of course, differ between the two models: R_{uv} near the wall, for example, approaches 0.34 for Model 1, and 0.21 for Model 2. But the limiting power-law exponents are precisely the same for the two models. It is noteworthy that the range of validity of the limiting power laws is quite different for different turbulence quantities: $u' \sim y$ out to Y of about 3 or 4, while $v' \sim y^2$ and $R_{uv} = \text{constant}$ out to Y of only about 0.3.

In general, the near-wall limiting behaviour for all variables extends to Y of about 0.3. Between $0.3 < Y < 3$, R_{uv} , v' and w' , especially for Model 2, depart considerably from their respective limiting near-wall power laws.

6.1. Physical explanation of limiting y^3 variation for \overline{uv}

By considering mass conservation near the wall, a simple physical explanation can be given for Reynolds stress varying as y^3 . Very near the wall the leading terms in

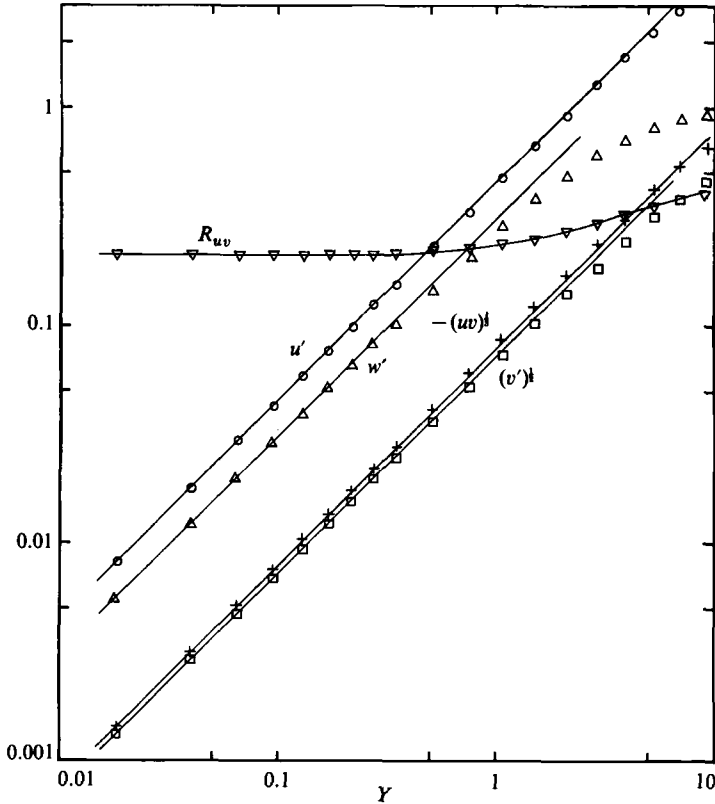


FIGURE 12. Near-wall behaviour of turbulence for Model 2: \circ , u' ; \square , $(v')^{1/2}$; \triangle , w' ; ∇ , R_{uv} ; $+$, $-(uv)^{1/2}$. Inclined straight lines are proportional to Y .

Taylor-series expansion for the fluctuating velocities are

$$u = a_1(x, z, t)y + \dots, \quad w = b_1(x, z, t)y + \dots \tag{19}$$

For mass conservation,

$$-\frac{\partial v}{\partial y} = \frac{\partial u}{\partial x} + \frac{\partial w}{\partial z} = \left(\frac{\partial a_1}{\partial x} + \frac{\partial b_1}{\partial z} \right) y + \dots,$$

so that integration, then multiplication by u and time averaging, yields

$$-\overline{uv} = \left(\frac{1}{2} \frac{\partial \overline{a_1^2}}{\partial x} + a_1 \frac{\partial \overline{b_1}}{\partial z} \right) \frac{y^3}{2} + \dots \tag{20}$$

Thus there clearly is a y^3 term in streamwise inhomogenous flows wherein $\overline{\partial a_1^2 / \partial x}$ is not zero. This point has never been in question. In streamwise homogenous flows, however, $\overline{\partial a_1^2 / \partial x}$ is zero and

$$-\overline{uv} = a_1 \frac{\partial \overline{b_1}}{\partial z} \frac{y^3}{2} + \dots = u \frac{\partial w}{\partial z} \frac{y}{2} + \dots, \tag{21}$$

from which it is seen that a leading y^3 term will also be present if u and $\partial w / \partial z$ (each of which is proportional to y) are positively correlated near the wall.

In a flow with positive Reynolds stress ($-\overline{uv} > 0$) sweep-type motions with $u > 0$

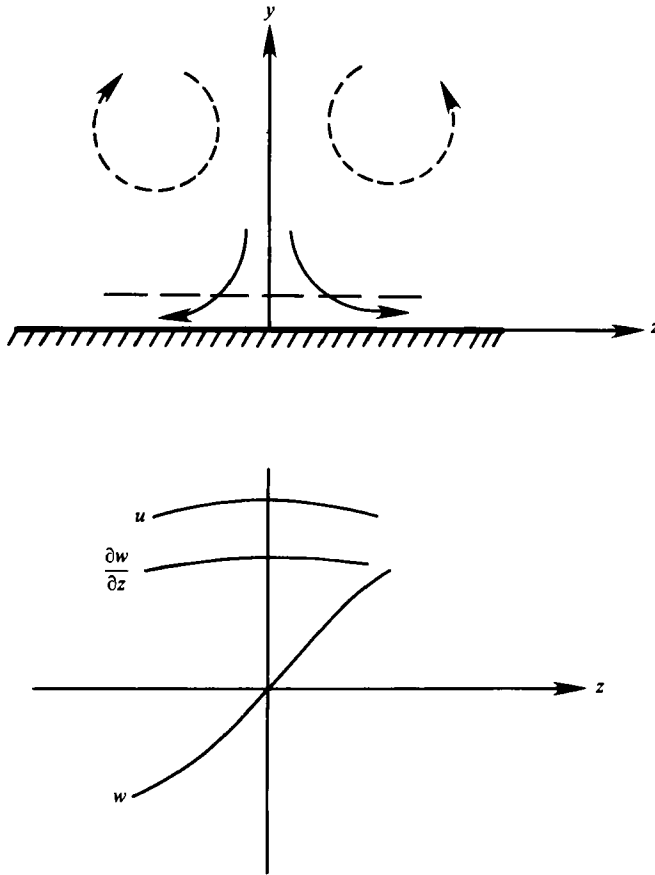


FIGURE 13. Sketch of wallward splatting eddy producing positive correlation between u and $\partial w/\partial z$. Sketched distributions of u , w and $\partial w/\partial z$ correspond to the y -value represented by the long-dashed line.

and $v < 0$ and/or ejection-type motions with $u < 0$ and $v > 0$ must dominate over motions yielding negative Reynolds stress (u and v of the same algebraic sign). The experimental data of Brodkey, Wallace & Eckelmann (1974) show that, as the wall is approached, the sweep-type motions increase in relative importance, producing twice the contribution to Reynolds stress that ejection-type motions do at $Y = 3$, the lower limit of their experimental data. Our numerical computations show the same trends. Hence, in determining whether or not u and $\partial w/\partial z$ are positively correlated near the wall, we consider first sweep-type motions, i.e. eddies moving wallward with $u > 0$.

A sketch of such a sweep-type motion, represented by a wallward moving eddy with $u > 0$, is shown in figure 13. Since the eddy cannot pass through the wall, it spreads in both directions spanwise ('splats') upon interacting with the wall. As the sketch illustrates, this bilateral spreading produces a positive $\partial w/\partial z$; and, since u is also positive, a positive correlation between u and $\partial w/\partial z$ results. With such correlation, conservation of mass (21) requires that the leading term in Reynolds stress be proportional to y^3 .

If ejection-type motions are considered, even though they contribute less to Reynolds stress, the signs of u and w are reversed, as are the directions of motion.

Hence u and $\partial w/\partial z$ are again positively correlated, and provide an additional y^3 contribution to \overline{uw} .

In the sketch of figure 13 two directions of contrarotating vortical motion compatible with the wallward splatting eddy are shown as dashed lines. Such vortical eddies may indeed be present, but they are not essential to the physical explanation.

It is to be noted that the simple physical explanation given for the y^3 limiting behaviour of Reynolds stress depends only on the continuity equation, and is independent of the Navier–Stokes momentum equations. The explanation would apply, for example, to non-Newtonian fluids as well as to one obeying the Navier–Stokes equations. It would also apply, for example, to curved as well as flat surfaces; and to flow with pressure gradient as well as without. Thus, we conclude that the y^3 limiting variation of Reynolds stress near a wall is very general indeed. Variations in the fluid momentum equations, pressure gradient, curvature, etc., will of course produce different values for the constant of proportionality in front of y^3 .

From the above considerations we can now understand how some previous theories have incorrectly yielded y^4 variations for \overline{uw} . Elrod (1957), for example, obtained the y^4 variation for streamwise homogenous flows through the erroneous assumption that, by symmetry, u and w (and their derivatives) are uncorrelated. In the Reynolds stress producing sweep motions, u and $\partial w/\partial z$ are strongly correlated; and this correlation produces a y^3 term. We believe that implicit in the theory of Ohji (1967), which yielded a y^4 variation for \overline{uw} , is an erroneous assumption equivalent to assuming that u and $\partial w/\partial z$ are uncorrelated. Monin & Yaglom (1971) have also noted that Ohji made a particular non-rigorous assumption not explicitly stated in his paper, although they do not identify what the wrong assumption was.

7. Applications to Reynolds-average turbulence modelling

The limiting behaviour of turbulence near a wall as defined by the computational models can be applied to strengthen certain aspects of Reynolds-average turbulence modelling. Two examples illustrating this are outlined in the paragraphs which follow. One pertains to the damping factors for Reynolds stress in eddy-viscosity models; and another to the wall boundary conditions for dissipation in k - ϵ models and stress-equation models.

7.1. Damping factors for eddy viscosity models

In eddy-viscosity (or mixing-length) models, the Reynolds stress near a wall is expressed as $-(\overline{uw})_+ = k^2 Y^2 D$, where $k = 0.4$ is the Kármán constant, and D is a ‘damping factor’ required to provide a smooth transition between the wall and the logarithmic region. The most widely used damping factor has been that of Van Driest (1956), namely $D_{\text{vd}} = (1 - e^{-Y/A})^2$, where A is a constant. Near a wall this yields $-(\overline{uw})_+ = k^2 Y^4/A^2$, unfortunately, an incorrect limiting behaviour. Van Driest obtained his damping factor by using Stokes flow of an oscillating plate under a stationary fluid to obtain $(1 - e^{-Y/A})$ as the damping factor for u -fluctuations; but he further assumed (incorrectly) that the v -fluctuations would be similarly damped, and thus obtained $(1 - e^{-Y/A})^2$ as the damping factor for Reynolds stress.

It is of interest that the correct near-wall behaviour of Reynolds stress is obtained if the analogy of oscillating-plate flow is adhered to for v as well as u -fluctuations. The incompressible v -velocity field for an infinite plate oscillating in the y -direction is not damped; hence the damping factor for oscillating plate flow is

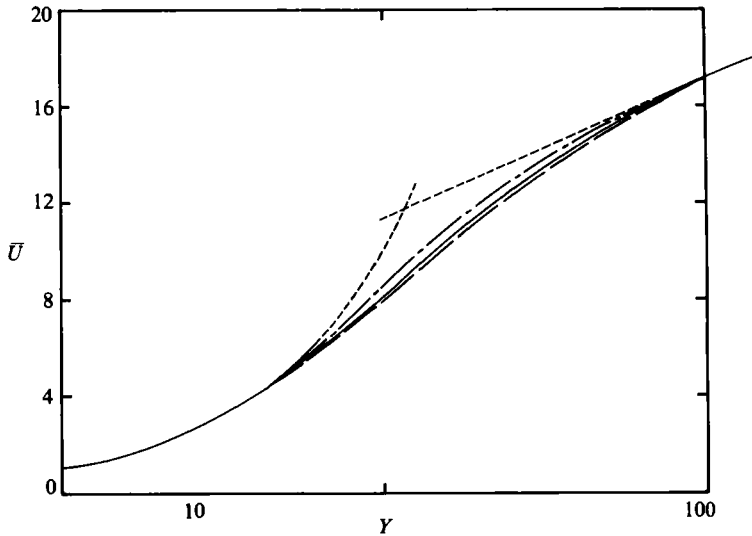


FIGURE 14. Law of the wall for three different eddy-viscosity damping factors: ——— vd = Van Driest; ----, op = oscillating plate flow; — · —, os = oscillating shear flow; · · · ·, $U = 5.6 + 5.75 \log Y$, and $\bar{U} = Y$.

$D_{op} = (1 - e^{-Y/A_{op}})$, where A_{op} is a constant. This yields the correct cubic power-law behaviour near a wall, $-(\overline{uv})_+ = k^2 y^3 / A_{op}$.

A still different damping factor is obtained from the analogy of oscillating shear flow over an infinite stationary wall (Chapman & Kuhn 1981). This type of flow seems more analogous to real flows than does the Stokes flow of an oscillating plate under a stationary fluid. In oscillating shear flow the u -fluctuations are damped as $D_{os} = (1 - 2 \cos \eta e^{-\eta} + e^{-2\eta})^{1/2}$, where $\eta \equiv Y/A_{os}$, and A_{os} is a constant. This damping factor applied to Reynolds stress also yields the correct cubic power-law behaviour near a wall, $-(\overline{uv})_+ = k^2 Y^3 \sqrt{2}/A_{os}$.

In each case the constants A , A_{op} and A_{os} are determined through a quadrature (Van Driest 1956) in which it is required that the logarithmic law of the wall for $\bar{U}(Y)$ is satisfied. Using $5.6 + 5.75 \log Y$ for the logarithmic region, the constants that fit this turn out to be $A = 27.8$, $A_{op} = 71.2$ and $A_{os} = 111$. As illustrated in figure 14, the resulting $\bar{U}(Y)$ -distributions are nearly the same irrespective of which damping factor is used.

Although the different damping factors yield similar results for \bar{U} , they yield very different results for \overline{uv} near a wall. For applications involving heat transfer in fluids with high Prandtl number, or diffusion in fluids with high Schmidt number, or the rate of deposition on a wall of small particles suspended in a turbulent flow, the near-wall values of \overline{uv} can be of central importance. The three different damping factors, when used in the simple eddy-viscosity (mixing-length) model of turbulence, yield the following results for Reynolds stress near a wall:

Damping factor	$-(\overline{uv})_+ / Y^3$ near wall
D_{vd} , Van Driest	0.0002 Y
D_{op} , oscillating plate flow	0.0022
D_{os} , oscillating shear flow	0.0020

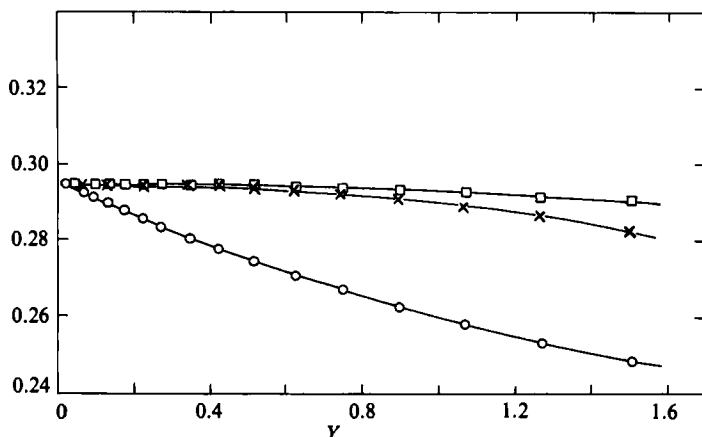


FIGURE 15. Near-wall behaviour of dissipation and related quantities in wall variables for Model 2: \circ , ϵ ; \square , $(6k/y^2 - (2/y)\partial k/\partial y)$; \times , $(4k/y^2) - \epsilon$.

By way of comparison, the corresponding results for the present computational models are:

Computational model	$-(\overline{uv})_+/Y^3$ near wall
Model 1	0.0007
Model 2	0.0005

7.2. Wall boundary condition for dissipation

In $k-\epsilon$ models, as well as in other models of turbulence that use an ϵ -transport equation, it is necessary to impose a boundary condition on ϵ at the wall. As summarized by Patel *et al.* (1981), three different boundary conditions have been employed in the past: $\epsilon_w = 0$; $(\partial\epsilon/\partial y)_w = 0$; and $(\epsilon)_w = (\partial^2 k/\partial y^2)_w$, or the equivalent $\epsilon_w = (2k/y^2)_w$, where $2k = (u'^2 + w'^2 + v'^2)$. A fourth wall boundary condition, $\epsilon_w = 2(\partial k^2/\partial y^2)_w$ has also been derived (Jones & Launder 1972) but to our knowledge has not been used in numerical computations. As a test of the first two of these, the near-wall behaviour in Models 1 and 2 of the mean value ϵ of the computed space- and time-dependent turbulence dissipation

$$\left[\left(\frac{\partial u}{\partial y}\right)^2 + \left(\frac{\partial w}{\partial y}\right)^2 + \left(\frac{\partial v}{\partial y}\right)^2 + \left(\frac{\partial u}{\partial z}\right)^2 + \left(\frac{\partial v}{\partial z}\right)^2 + \left(\frac{\partial w}{\partial z}\right)^2 \right]$$

is shown in figure 15 in wall variables. It is clear that $\epsilon_w = 0$ is incorrect (as is well known), and that $(\partial\epsilon/\partial y)_w = 0$ is also incorrect. That the third boundary condition is a correct one follows directly from the limiting near-wall behaviour of u' and w' (Jones & Launder 1972). Moreover an alternate boundary condition for ϵ_w that does not involve $\partial^2 k/\partial y^2$, but only a first derivative, can also be derived. We have, using wall variables,

$$\begin{aligned} u &= a_1 y + a_2 y^2 + O(y^3), \\ w &= b_1 y + b_2 y^2 + O(y^3), \\ v &= c_2 y^2 + O(y^3), \end{aligned}$$

where the coefficients a_1 , a_2 , b_1 , b_2 , and c_2 are functions of x , z and t . Hence, $2k/y^2 = (\overline{a_1^2 + b_1^2}) + 2(\overline{a_1 a_2 + b_1 b_2})y + O(y^2)$. Disregarding the very small contribution to

ϵ of spanwise derivatives (which are zero at the wall), we have

$$\begin{aligned}\epsilon &= \overline{\left(\frac{\partial u}{\partial y}\right)^2} + \overline{\left(\frac{\partial w}{\partial y}\right)^2} + \overline{\left(\frac{\partial v}{\partial y}\right)^2} = \overline{(a_1 + 2a_2 y)^2} + \overline{(b_1 + 2b_2 y)^2} + O(y)^2 \\ &= (\overline{a_1^2} + \overline{b_1^2}) + 4(\overline{a_1 a_2} + \overline{b_1 b_2})y + O(y^2),\end{aligned}$$

from which it follows that $\epsilon_w = (\partial^2 k / \partial y^2)_w = (\overline{a_1^2} + \overline{b_1^2})$, and that near the wall ($\epsilon - \epsilon_w$) varies linearly with y . It also readily follows from manipulation of the above equations that the r.m.s. streamwise and spanwise vorticity intensity varies similarly, e.g. $(\Omega'_x - \Omega'_{xw}) \sim y$ and $(\Omega'_z - \Omega'_{zw}) \sim y$; but that the r.m.s. normal vorticity intensity $\Omega'_y \sim y$ since $\Omega'_{yw} = 0$.

With $C \equiv (\overline{a_1 a_2} + \overline{b_1 b_2})$, it follows that the first two terms in the near-wall expansion are

$$\epsilon = \epsilon_w + 4Cy, \quad \frac{2k}{y^2} = \epsilon_w + 2Cy.$$

From these two equations there follow some alternative near-wall limiting equations for dissipation valid within the small but finite Y -range of limiting near-wall behaviour:

$$\epsilon_w = \frac{6k}{y^2} - \frac{2}{y} \frac{\partial k}{\partial y}, \quad \frac{\partial \epsilon}{\partial y} = \left(\frac{\partial \epsilon}{\partial y}\right)_w, \quad \epsilon_w = \frac{4k}{y^2} - \epsilon.$$

As illustrated in figure 15, the quantity $6k/y^2 - (2/y)\partial k/\partial y$ is very nearly constant near the wall. It is equal to the wall dissipation $(\epsilon_+)_w$ to within 0.1% up to about $Y = 0.6$, and within 1% up to about $Y = 1.3$. The quantity $\partial \epsilon / \partial y$ is nearly constant up to about $Y = 0.3$. The quantity $(4k/y^2) - \epsilon$ in the numerical computations is equal to the wall dissipation to within 1% up to about $Y = 0.8$. For some numerical algorithms, a boundary condition involving only a first derivative, or no derivative, is preferable to one involving a second derivative. The last equation listed above probably provides the simplest wall boundary condition for use in numerical computations of the ϵ -transport equation. In terms of known values k_1 and ϵ_1 at the first mesh point away from the wall (located at a Y_1 of less than about 0.6 wall units), the wall boundary condition in wall variables is simply $\epsilon_w = (4k_1/y_1^2) - \epsilon_1$.

7.3. Damping factor for Kolmogorof-Prandtl relationship in k - ϵ models

In k - ϵ models of turbulence, the Kolmogorof-Prandtl relationship between turbulent kinematic viscosity ν_t , dissipation ϵ and kinetic energy k , is taken as

$$\frac{-\overline{uv}}{\partial \overline{u} / \partial y} = \nu_t = \frac{f_\mu C \rho k^2}{\epsilon},$$

where C is a constant, and f_μ is a damping factor inserted to yield a correct equation as the wall is approached. Since $-\overline{uv} \sim y^3$, $k \sim y^2$, and $\epsilon \rightarrow \epsilon_w$ as $y \rightarrow 0$, it follows that f_μ would have to vary as y^{-1} near the wall. Among the various *ad hoc* f_μ damping functions used in the eight different k - ϵ models surveyed by Patel *et al.* (1981), none corresponds to a y^{-1} variation near the wall.

8. Concluding remarks

Three different computational models for incompressible viscous-sublayer turbulence have been developed and employed to investigate the limiting variation of turbulence near a wall. They are characterized by different velocity boundary conditions imposed on the time-dependent Navier-Stokes equations at the outer

edge of the viscous sublayer. Although these boundary conditions differ significantly, they yield surprisingly similar results for most of the turbulence quantities. All models, for example, yield reasonably realistic computations of mean streamwise velocity, Reynolds stress, u - v correlation coefficient, and the fluctuating intensities of velocity and Reynolds stress. Relative to Model 1, which is the simplest, the principal merit of Model 2 is that it yields more realistic values for the skewness and flatness factors near the wall. Model 3, which requires much more computation time than either Model 1 or 2, does not appear to yield significant improvement over Model 2, and relatively little over Model 1.

All three models exhibit near the outer edge of the viscous sublayer a thin region in which velocity gradients vary rapidly from anomalously high values at the outer edge ($Y = 40$) to reasonably realistic values at Y -values of about 30–35. In this thin, outer Stokes-layer region, both the rate of turbulent energy dissipation and the r.m.s. fluctuations in streamwise vorticity are anomalously high. This is the principal inaccuracy of the models. The outer-edge anomaly is attributed to some unrealistic aspect of the small-scale eddy structure in the boundary conditions. This anomaly is believed not to affect conclusions about the limiting near-wall power-law behaviour of turbulence.

The limiting third-power variation of Reynolds stress near a wall is concluded to be very general because of the physical explanation underlying it. In essence, wallward splatting eddies that produce the principal Reynolds stress near a wall also produce positive correlation between u and $\partial w/\partial z$, and this requires a y^3 variation to conserve mass. Since this physical explanation applies equally to Newtonian or non-Newtonian fluids, to flows with or without pressure gradient, and to curved or flat walls, the y^3 variation is concluded to be very general. The constant of proportionality, of course, may depend upon such variables; but the cubic variation will not.

It is noted that the limiting power laws for several of the turbulence quantities are accurate only for Y less than about 0.3, while for other quantities it extends out to larger values of Y . This is a surprisingly small domain. In the range $0.3 < Y < 3$, power laws are still a good approximation, but the exponents change a little: to less than 1 for w' , less than 2 for v' , and to slightly greater than 3 for \overline{uv} . The u - v correlation varies considerably over this range.

The observed limiting behaviour of various turbulence quantities near a wall, as reflected in the exponent of their limiting power-law behaviour, is summarized as follows:

$$\begin{aligned} \text{No variation, } R_{uv}, & \frac{u'}{\langle U \rangle}, \frac{w'}{\langle U \rangle}, \left(\frac{4k}{y}\right)^2 - \epsilon, \left(\frac{6k}{y^2}\right) - \frac{2\partial k}{y\partial y}; \\ y \text{ variation } & u', \frac{v'}{\langle U \rangle}, w', (\Omega'_x - \Omega'_{zw}), \Omega'_y, (\Omega'_z - \Omega'_{zw}), (\epsilon - \epsilon_w); \\ y^2 \text{ variation } & v'; \\ y^3 \text{ variation } & \langle uv \rangle. \end{aligned}$$

This research was sponsored by the Office of Naval Research under Contract N00014-82-C-0672. Acknowledgement is gratefully made to the NASA Ames Research Center for providing the necessary computing time and to Drs John Kim and Parviz Moin who furnished the basic Navier–Stokes code, and who, together with Dr Phillippe Spalart, participated in many helpful technical discussions during the course of the research.

REFERENCES

- ANDREOPOULOS, J., DURST, F. & JOVANOVIC, J. 1983 On the structure of turbulent boundary layers at different Reynolds numbers. In *4th Intl Symp. on Turbulent Shear Flows, Karlsruhe, W. Germany*, pp. 2.1–2.5.
- BADRI NARAYANAN, M. A. & MARVIN, J. G. 1978 On the period of coherent structure in boundary layers at large Reynolds numbers. *NASA TM 78477*.
- BAKEWELL, H. P. & LUMLEY, J. L. 1967 Viscous sublayer and adjacent wall region in turbulent pipe flow. *Phys. Fluids* **10**, 1880–1889.
- BANDYOPADHYAY, P. R. 1982 Period between bursting in turbulent boundary layers. *Phys. Fluids* **25**, 1751–1754.
- BLACKWELDER, R. F. & ECKELMANN, H. 1979 Streamwise vortices associated with the bursting phenomenon. *J. Fluid Mech.* **94**, 577–594.
- BLACKWELDER, R. F. & HARITONIDIS, J. H. 1983 Reynolds number dependence of the bursting frequency in turbulent boundary layers. *J. Fluid Mech.* **132**, 87–103.
- BLACKWELDER, R. F. & KAPLAN, R. E. 1976 On the wall structure of the turbulent boundary layer. *J. Fluid Mech.* **76**, 89–112.
- BRODKEY, R. S., WALLACE, J. M. & ECKELMANN, H. 1974 Some properties of truncated turbulence signals in bounded shear flows. *J. Fluid Mech.* **63**, 209–224.
- BROWN, G. L. & THOMAS, A. S. W. 1977 Large structure in a turbulent boundary layer. *Phys. Fluids* **20**, S243–S252.
- CANTWELL, B., COLES, D. & DIMOTAKIS, P. 1978 Structure and entrainment in the plane of symmetry of a turbulent spot. *J. Fluid Mech.* **87**, 641–672.
- CHAPMAN, D. R. & KUHN, G. D. 1981 Two-component Navier–Stokes computational model of viscous sublayer turbulence. *AIAA Paper* 81–1024.
- CHAPMAN, D. R. & KUHN, G. D. 1984 Computational models of the viscous sublayer and limiting behavior of turbulence near a wall. *Nielsen Engineering & Research, Inc. TR-334*, December 1984.
- CHEN, C. H. & BLACKWELDER, R. 1978 Large-scale motion in a turbulent boundary layer: a study using temperature contamination. *J. Fluid Mech.* **89**, 1–31.
- CLARK, J. A. 1968 A Study of turbulent boundary layers in channel flow. *Trans. ASME D: J. Basic Engng* **90**, 455–465.
- CLARK, J. A. & MARKLAND, E. 1969 Vortex structures in turbulent boundary layers. *Aero. J.* **74**, 243–244.
- COLES, D. 1985 The uses of coherent structure. *AIAA Paper* 85–0507.
- CORINO, E. R. & BRODKEY, R. S. 1969 A visual investigation of the wall region in turbulent flow. *J. Fluid Mech.* **37**, 1–30.
- DONOHUE, G. L., TIEDERMAN, W. G. & REISCHMAN, M. M. 1972 Flow visualization of the near-wall region in a drag-reducing channel flow. *J. Fluid Mech.* **56**, 559–575.
- ECKELMANN, H. 1974 The structure of the viscous sublayer and the adjacent wall region in a turbulent channel flow. *J. Fluid Mech.* **65**, 439–459.
- ELENA, M. 1977 Etude expérimentale de la turbulence on voisinage de la paroi d'un tube légèrement chauffé. *Intl J. Heat Mass Transfer* **20**, 935–944.
- ELENA, M., FULACHIER, D. & DUMAS, R. 1979 Etude expérimentale des apports et des éjections de fluide dans une couche limitée turbulent. *AGARD CPP271*, pp. 2–1–2–21.
- ELROD, H. G. 1957 Note on the turbulent shear stress near a wall. *J. Aero. Sci.* **24**, 468–469.
- FALCO, R. E. 1977 Coherent motions in the outer region of turbulent boundary layers. *Phys. Fluids* **20**, S124–S132.
- FULACHIER, L. 1972 Contribution à l'étude des analogies des champs dynamique et thermique dans une couche limite turbulent. Effect de l'aspiration. Thesis, University of Provence, France.
- GRASS, A. J. 1971 Structural features of turbulent flow over smooth and rough surfaces. *J. Fluid Mech.* **50**, 233–255.
- GUPTA, A. K. & KAPLAN, R. E. 1972 Statistical characteristics of Reynolds stress in a turbulent boundary layer. *Phys. Fluids* **15**, 981–985.

- GUPTA, A. K., LAUFER, J. & KAPLAN, R. E. 1971 Spatial structure in the viscous sublayer. *J. Fluid Mech.* **50**, 493–512.
- HATZIAVRAMIDIS, D. T. & HANRATTY, T. J. 1979 The representation of the viscous wall region by a regular eddy pattern. *J. Fluid Mech.* **95**, p. 655.
- HINZE, J. O. 1975 *Turbulence*, 2nd edn, p. 621. McGraw-Hill.
- HIRATA, M., TANAKA, H., KAWAMURA, H. & KASAGI, N. 1982 Heat transfer in turbulent flows. In *Proc. Seventh Intl Heat Transfer Conference, München*, 6–10 Sept. 1982, vol. 1, pp. 31–57. Hemisphere.
- HOGENES, J. H. A. & HANRATTY, T. J. 1982 The use of multiple wall probes to identify coherent flow patterns in the viscous wall region. *J. Fluid Mech.* **124**, 363.
- HUSSAIN, A. K. M. F. & REYNOLDS, W. C. 1975 Measurements in fully developed turbulent channel flow. *Trans. ASME I: J. Fluids Engrg* **97**, 568–578.
- IRITANI, Y., KASAGI, N. & HIRATA, M. 1983 Heat transfer mechanism and associated turbulence structure in the near-wall region of a turbulent boundary layer. In *4th Int. Symp. on Turbulent Shear Flows, Karlsruhe, W. Germany*, pp. 17.31–17.36.
- JOHANSSON, A. V. & ALFREDSSON, P. H. 1982 On the structure of turbulent channel flow. *J. Fluid Mech.* **122**, 295–314.
- JONES, W. P. & LAUNDER, B. E. 1972 The prediction of laminarization with a two-equation model. *Intl J. Heat Mass Transfer* **15**, 301–314.
- KANEDA, Y. & LESLIE, D. C. 1982 Tests of subgrid models in the near-wall region using represented velocity fields. *J. Fluid Mech.* **132**, 349–373.
- KASAGI, N., HIRATA, M. & NISHINO, K. 1984 Streamwise pseudo-vortical structures and associated vorticity in the near-wall region of a wall-bounded turbulent shear flow. *9th Biennial Symposium on Turbulence, Univ. of Missouri-Rolla, Rolla, Missouri*. Univ. of Missouri-Rolla, Department of Chemical Engineering.
- KASTRINAKAS, E. G. & ECKELMANN, H. 1983 Measurement of streamwise vorticity fluctuations in a turbulent channel flow. *J. Fluid Mech.* **137**, 165–186.
- KASTRINAKAS, L., WALLACE, J. M. & WILLMARTH, W. W. 1975 Measurements of small scale streamwise vorticity in a turbulent channel flow. *Bull. Am. Phys. Soc.* **20**, 1422.
- KIM, J. 1983 On the structure of wall bounded turbulent flows. *Phys. Fluids* **26**, 2088–2097.
- KIM, J. 1985 Turbulence structures associated with the bursting event. *Phys. Fluids* **28**, 52–58.
- KIM, H. T., KLINE, S. J. & REYNOLDS, W. C. 1971 The production of turbulence near a smooth wall in a turbulent boundary layer. *J. Fluid Mech.* **50**, 133–160.
- KIM, J. & MOIN, P. 1984 A factored fractional step numerical method for incompressible Navier–Stokes equations. *NASA TM 85898*.
- KLINE, S. J., REYNOLDS, W. C., SCHRAUB, P. A. & RUNSTADLER, P. W. 1967 The structure of turbulent boundary layers. *J. Fluid Mech.* **30**, 741–773.
- KOVASNAY, L. S. G., KIBENS, V. & BLACKWELDER, R. 1970 Large scale motion in the intermittent region of a turbulent boundary layer. *J. Fluid Mech.* **41**, 283–325.
- KREPLIN, H. P. & ECKELMANN, H. 1979 Propagation of perturbations in the viscous sublayer and adjacent wall region. *J. Fluid Mech.* **95**, 305–322.
- KUTATELADZE, S. S., KHABAKHPASHEVA, E. M., ORLOV, V. V., PEREPELTSIA, B. V. & MIKHAILOVA, E. S. 1977 Experimental investigation on the structure of near-wall turbulence and viscous sublayer. In *Symp. on Turbulent Shear Flows, Pennsylvania State University, 1977*, pp. 91–103. Springer.
- LAUFER, J. 1950 Investigation of turbulent flow in a two-dimensional channel. *NACA TN 2123*.
- LAUFER, J. 1954 The structure of turbulence in fully developed pipe flow. *NACA TN 1174*.
- LEE, M. K., ECKELMANN, L. & HANRATTY, T. J. 1974 Identification of turbulent wall eddies through the phase relationship of the components of the fluctuating velocity gradient. *J. Fluid Mech.* **66**, 17–33.
- LU, S. S. & WILLMARTH, W. W. 1973 Measurements of the structure of the Reynolds stress in a turbulent boundary layer. *J. Fluid Mech.* **60**, 481–511.
- MOIN, P. & KIM, J. 1982 Numerical investigation of turbulent channel flow. *J. Fluid Mech.* **118**, 341–377.
- MONIN, A. S. & YAGLOM, A. M. 1971 *Statistical Fluid Mechanics*, vol. 1 (English edn). M.I.T. Press.

- MOSE, R. D. & MOIN, P. 1984 Direct numerical simulation of curved channel flow. *Rep. Stanford Univ. Dept. of Mech. Engrg*, TF-20.
- NAKAGAWA, H. & NEZU, I. 1981 Structure of space-time correlations of bursting phenomena in an open-channel flow. *J. Fluid Mech.* **104**, 1-43.
- NIKOLAIDES, C. 1984 A Study of coherent structures in the viscous wall region of a turbulent flow. Ph.D. thesis, University of Illinois, Urbana.
- NIKOLAIDES, C. & HANRATTY, T. J. 1983 Computer simulation of the time varying velocity field in the viscous wall region. In *4th Intl Symp. on Turbulent Shear Flows, Karlsruhe, W. Germany*, pp. 3.21-3.24.
- NYCHAS, S. G., HERSHEY, H. C. & BRODKEY, R. S. 1973 A visual study of turbulent shear flow. *J. Fluid Mech.* **61**, 513-540.
- OFFEN, G. R. & KLINE, S. J. 1975 A proposed model of the bursting process in turbulent boundary layers *J. Fluid Mech.* **70**, 209-228.
- OHJI, M. 1967 Statistical theory of wall turbulence. *Phys. Fluids* **10**, S153-S154.
- PATEL, V. C., RODI, W. & SCHEUERER, G. 1981 Evaluation of turbulence models for near-wall and low-Reynolds number flows. In *3rd Intl Symp. on Turbulent Shear Flows, University of California Davis*, pp. 1.1-1.8.
- PRATURI, A. K. & BRODKEY, R. S. 1978 A stereoscopic visual study of coherent structures in turbulent shear flow. *J. Fluid Mech.* **89**, 251-272.
- REICHARDT, H. 1951 Vollständige Darstellung der Turbulenten Geschwindigkeitsverteilung in Glatten Leitungen. *Z. Angew. Math. Mech.* **31**, 208-219.
- SCHILDKNECHT, M., MILLER, J. A. & MEIER, G. E. A. 1979 The influence of suction on the structure of turbulence in fully developed pipe flow. *J. Fluid Mech.* **90**, 67-107.
- SCHRAUB, F. A. & KLINE, S. J. 1965 A study of the structure of the turbulent boundary layer with and without longitudinal pressure gradients. *Rep. Stanford Univ. Dept. of Mech. Engrg*, MD-12.
- SMITH, C. R. 1978 Visualization of turbulent boundary layer structure using a moving hydrogen bubble-wire probe. *AFOSR/Lehigh University Workshop*.
- UEDA, H. & HINZE, J. O. 1975 Fine-structure turbulence in the wall region of a turbulent boundary layer. *J. Fluid Mech.* **67**, 125-143.
- VAN DRIEST, E. R. 1956 On turbulent flow near a wall. *J. Aero. Sci.* **23**, 1007-1011.
- WALLACE, J. M., BRODKEY, R. S. & ECKELMANN, H. 1977 Pattern recognized structures in bounded turbulent shear flows. *J. Fluid Mech.* **83**, 673-693.
- WALLACE, J. M., ECKELMANN, H. & BRODKEY, R. S. 1972 The wall region in turbulent flow. *J. Fluid Mech.* **54**, 39-48.
- WILLMARTH, W. W. 1975 Structure of turbulent boundary layers. *Adv. Appl. Mech.* **15**, 159-254.